Chemical Science

ROYAL SOCIETY OF CHEMISTRY

EDGE ARTICLE

View Article Online
View Journal | View Issue

Cite this: *Chem. Sci.*, 2025, **16**, 17241

All publication charges for this article have been paid for by the Royal Society of Chemistry

Received 18th June 2025
Accepted 12th August 2025

DOI: 10.1039/d5sc04467g

rsc.li/chemical-science

Observation of competing nitrogen activation in metal tricarbon anions MC_3^- (M = Os, Ir, Pt)

Shihu Du,†[ab] Ziheng Zhang,†[a] Gang Li,[a] Shibo Cheng,[b] Xiangtao Kong,[c] Lu Li,[d] Qinqin Yuan,[e] Hua Xie *[a] and Ling Jiang[a]

Metal carbides hold significant potential as catalytic and functional materials. However, the absence of explicit directives hinders investigations of the reaction mode of metal carbide clusters. In this study, we employ size-specific photoelectron velocity-map imaging spectroscopy to explore the reactivity of metal tricarbon clusters MC_3^- (M = Os, Ir, Pt) in nitrogen activation. The experimental results reveal two competing modes of nitrogen activation: cleavage of the N≡N bond with formation of a stable C–N bond, and chemisorption. IrC_3^- exhibits coexistence of dual nitrogen activation mechanisms, while OsC_3^- achieves nitrogen activation through cleavage of the N≡N bond and PtC_3^- employs chemisorption-mediated activation of dinitrogen. Further theoretical analysis suggests that the activation of N_2 by MC_3^- (M = Os, Ir, Pt) decreases as the 5d orbital energy of the metal atoms decreases. Additionally, the chemisorption mode becomes more dominant, consistent with the experimental results. These findings are promising for advancing nitrogen activation and have important implications for the development of related single-atom catalysts with isolated metal atoms dispersed on supports.

Introduction

Most nitrogen-containing compounds are synthesized from NH_3 and the traditional Haber–Bosch process operates under harsh conditions. The effective conversion and activation of nitrogen under mild conditions remain quite challenging in the chemical industry.[1–5] Ongoing efforts focus on understanding the catalytic conversion of nitrogen to NH_3 through various transition metal complexes.[6–14] Studying individual active species confined within metal clusters under isolated, controlled, and reproducible conditions is an ideal method for elucidating mechanistic details and key factors at the molecular level.[15–18] This method provides insights into the significant catalytic efficiency and reaction selectivity of metal clusters. For example, the binding of N_2 to some metal atom dimers (*e.g.*, Ti_2, Sc_2, Gd_2, and Ta_2^+),[19–22] and some transition metal clusters (*e.g.*, Ta_2N^+, $Ta_3N_3H_{0,1}^-$, and $V_5N_5^-$)[23–26] results in significant N≡N bond activation. Furthermore, the d orbital energies of metal elements typically decrease from left to right across the periodic table, which may decrease the interaction between the orbitals of the N_2 ligand and those of later transition metals,[27] as confirmed by a previous study on bare metal clusters.[10]

Furthermore, transition metal carbides possess immense potential for applications in catalytic and functional materials, and considerable achievements have been made in the study of their structure and reactivity.[28–31] Metal carbide clusters play a crucial role in the activation of N_2; for instance, the transition metal carbide clusters $FeV_2C_2^-$, $FeTaC_2^-$, $Ta_2C_4^-$, $V_3C_4^-$, V_3C^+, and $V_{3-x}Ta_xC_4^-$ (x = 0–3)[32–37] can completely cleave the N≡N triple bond and form stable C–N bonds. The formation of C–N bonds allows the incorporation of nitrogen into organic molecules. Such C–N compounds, as fundamental components of natural products, medicinal compounds, and multifunctional materials, are important in this field of research,[38] and C–N metal clusters can be formed *via* reactions between nitrogen and carbon dioxide under suitable conditions.[39–41]

Given the important role of metal carbide clusters, this article provides a detailed analysis of the noteworthy competing relationship between the two modes of nitrogen activation exhibited by metal tricarbon compounds, MC_3^- (M = Os, Ir, Pt), which is intimately connected to the d-orbital energy of the metal atom.

Experimental and computational methods

Experiments were conducted using a custom-built instrument that incorporated a laser vaporization source and a dual-

[a]State Key Laboratory of Chemical Reaction Dynamics, Dalian Institute of Chemical Physics, Chinese Academy of Sciences, 457 Zhongshan Road, Dalian 116023, China. E-mail: xiehua@dicp.ac.cn

[b]School of Chemistry and Chemical Engineering, Shandong University, Jinan 250100, China

[c]Henan Key Laboratory of New Optoelectronic Functional Materials, College of Chemistry and Chemical Engineering, Anyang Normal University, Anyang 455000, China

[d]Department of Criminal Science and Technology, Liaoning Police College, Dalian 116036, China

[e]Department of Chemistry, Key Laboratory of Functional Inorganic Materials of Anhui Province, Anhui University, Hefei 230601, China

† These authors contributed equally to this work.

channel time-of-flight mass spectrometer. Details of the apparatus have been provided elsewhere,[42] and only a brief description is given below. MC_3^- and $MC_3N_2^-$ (M = Os, Ir, Pt) anions were produced by laser vaporization of M–C (M = Os, Ir, Pt) mixtures (mole ratio, M/C = 1 : 4) in the presence of a helium carrier gas seeded with 5% N_2. The typical stagnation pressure of the carrier gas was approximately 2–5 atm. After the samples were cooled and expanded into the source chamber, the anions of interest were mass selected using a Wiley–McLaren time-of-flight mass spectrometer and then introduced into the photodetachment region, where they interacted with laser beams operating at 266 nm (4.661 eV). The photoelectrons were mapped onto a detector consisting of a microchannel plate and a phosphor screen. The two-dimensional (2D) images on the phosphor screen were recorded using a charge-coupled device camera. Each image was obtained by accumulating 10 000–50000 laser shots at a repetition rate of 10 Hz. All raw images were reconstructed using the basis set expansion (BASEX) inverse Abel transform method. The photoelectron spectra were calibrated using the known spectrum of Au^-.[43] The energy resolution was better than 5%, corresponding to 50 meV at an electron kinetic energy (eKE) of 1 eV.

To elucidate the electronic and geometrical structures of $MC_3N_2^-$ (M = Os, Ir, Pt), theoretical calculations were conducted using the Gaussian 09 program.[44] The structures were optimized *via* density functional theory using the B3LYP functional together with the aug-cc-pVTZ basis set for C and N and the aug-cc-pVTZ-PP basis set for the M atom (M = Os, Ir, Pt).[45–47] Harmonic frequency analysis was performed to ensure that the obtained structures corresponded to real minima on the potential energy surfaces. The vertical detachment energy (VDE) was calculated as the difference in energy between the neutral and anionic species based on the optimized anionic geometry, and the adiabatic detachment energy (ADE) was calculated as the difference in energy between the neutral and anionic species in their optimized geometries. Zero-point-energy corrections were considered in the total energy of each cluster isomer used for the relative energy and ADE calculations. To understand the structure of $MC_3N_2^-$ (M = Os, Ir, Pt), the Wiberg bond orders, bond lengths, and bond angles of $MC_3N_2^-$ (M = Os, Ir, Pt) were determined, and natural population analysis (NPA) and canonical molecular orbital (CMO) analysis were performed by means of the Gaussian 09 package.

Results and analysis

The photoelectron spectra of MC_3^- and $MC_3N_2^-$ (M = Os, Ir, Pt) recorded at 266 nm are shown in Fig. 1. The structures of IrC_3^- and PtC_3^- have been determined in previous studies.[30] In addition, structure optimization and a comparison of the theoretical simulation results with experimental results shown in Fig. S1 and S2 indicated that OsC_3^- adopted a linear chain configuration (similar to IrC_3^- and PtC_3^-). The electron binding energy of the maximum of each 1st resolved band (labeled with X) corresponded to the VDEs of the ground state, as shown in Fig. 1, which were directly measured to be 2.98 ± 0.08 eV, 3.18 ± 0.07 eV, and 2.58 ± 0.10 eV for $MC_3N_2^-$ with M = Os, Ir, and Pt,

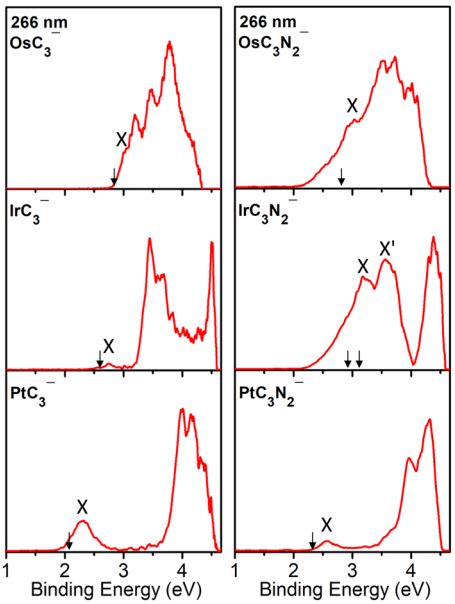

Fig. 1 Photoelectron spectra of MC_3^- and $MC_3N_2^-$ (M = Os, Ir, Pt) at 266 nm (4.661 eV). Mark X represents the vertical detachment energy, and the black arrow represents the experimentally estimated adiabatic detachment energy.

respectively (Table 1). Bands in the spectra without vibrational structures prevented us from directly measuring the ground-state ADEs, so these values were instead estimated by drawing a straight line at the rising edge of the main band and adding the instrumental resolution to the point of intersection with the binding energy axis. The ADE values (black arrow marking) corresponding to the X bands for $MC_3N_2^-$ (M = Os, Ir, Pt) were determined to be 2.80 ± 0.09 eV, 2.95 ± 0.08 eV, and 2.35 ± 0.12 eV (Table 1), respectively.

To assign the observed spectral features and determine the structures of the low-lying isomers, quantum chemical calculations at the B3LYP/aug-cc-pVTZ/aug-cc-pVTZ-PP level of theory were performed for $MC_3N_2^-$ (M = Os, Ir, Pt). The optimized structures of the three lowest-energy isomers for the $MC_3N_2^-$ (M

Table 1 Comparison of the experimental VDE and ADE values with the B3LYP calculated ones for the three lowest-energy isomers of $MC_3N_2^-$ (M = Os, Ir, Pt)

Cluster	Isomer	Relative energy (eV)	VDE (eV)		ADE (eV)	
			Expt.[a]	Calc.	Expt.[a]	Calc.
$OsC_3N_2^-$	3A	0.00	2.98 (8)	2.93	2.80 (9)	2.81
	3B	1.46		3.30		3.20
	3C	1.93		2.83		2.66
$IrC_3N_2^-$	3a	0.00	3.18 (7)	3.12	2.95 (8)	3.02
	3b	0.33	3.55 (6)	3.50	3.10 (8)	3.21
	3c	0.97		3.56		3.12
$PtC_3N_2^-$	3I	0.00	2.58 (10)	2.56	2.35 (12)	2.43
	3II	0.47		3.66		3.47
	3III	0.50		2.75		2.59

[a] Numbers in parentheses represent the uncertainty in the last digit.

= Os, Ir, Pt) anions are shown in Fig. 2. Other low-lying isomers are illustrated in Fig. S3–S5. The theoretical VDEs and ADEs of the three lowest-energy isomers are listed and compared with the experimentally measured values in Table 1. The density of states spectra of the isomers were simulated on the basis of the theoretically generalized Koopman's theorem and are compared with the experimental spectra in Fig. 3.

$OsC_3N_2^-$

In the most stable isomer (3A) of $OsC_3N_2^-$, N_2 was completely cleaved (referred to as the breaking configuration). Isomer 3B, in which N_2 was bound to the Os atom in an end-on configuration at a certain angle, was 1.46 eV higher in energy than isomer 3A. Isomer 3C, in which N_2 was bound to the Os atom in a side-on configuration at a certain angle, was 1.93 eV higher in energy than isomer 3A. Isomers 3A, 3B and 3C were characterized by C_s symmetry and a $^2A'$ electronic state.

The calculated VDE and ADE values of isomer 3A (2.93 eV and 2.81 eV) agreed well with the experimental values (2.98 ± 0.08 eV and 2.80 ± 0.09 eV) (Table 1). In contrast the calculated VDE and ADE values of isomer 3B (3.30 eV and 3.20 eV) were obviously higher than the experimental values, whereas those of 3C (2.83 eV and 2.66 eV) were much lower than the experimental values. As shown in Fig. 3, the simulated spectrum of isomer 3A agreed best with the experimental spectrum, confirming that the experimental spectrum could be attributed to isomer 3A. Thus, the presence of isomers 3B and 3C can be ruled out.

$IrC_3N_2^-$

For $IrC_3N_2^-$, the structures of isomers 3a, 3b, and 3c were similar to those of isomers 3A (breaking configuration), 3B (end-on configuration), and 3C (side-on configuration), respectively. As listed in Table 1, the calculated VDE and ADE values of the lowest-lying isomer (3a) were 3.12 eV and 3.02 eV, respectively, in excellent agreement with the experimental results (3.18 ± 0.07 and 2.95 ± 0.08 eV). Isomer 3b was only 0.33 eV higher in energy than isomer 3a. The calculated VDE and ADE values of isomer 3b (3.50 eV and 3.21 eV) agreed well with the VDE and ADE (3.55 ± 0.06 eV and 3.10 ± 0.08 eV) corresponding to the 2nd resolved band (marked as X′) of the experimental spectra. Isomer 3c (with calculated VDE and ADE values of 3.56 eV and 3.12 eV, respectively) was 0.97 eV higher in energy than isomer 3a, and was too high in energy to be experimentally probed. As shown in Fig. 3, the best agreement between the simulated and experimental spectra was achieved when a mixture of isomers 3a and 3b was assumed, implying the coexistence of these two isomers.

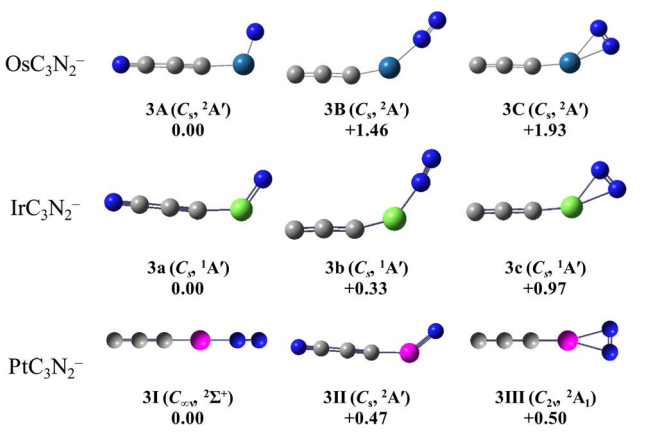

Fig. 2 Optimized structures of the three low-energy isomers for $MC_3N_2^-$ (M = Os, Ir, Pt). Relative energies are given in eV.

$PtC_3N_2^-$

For $PtC_3N_2^-$, the most stable isomer (3I), exhibited a linear chain structure in which N_2 was bound to the Os atom in an end-on $C_{\infty v}$ configuration and had a $^2\Sigma^+$ ground state. The calculated VDE and ADE values of isomer 3I were 2.56 eV and 2.43 eV (Table 1), respectively, consistent with the corresponding experimental values (2.58 ± 0.10 eV and 2.35 ± 0.12 eV). Isomer 3II was 0.47 eV higher in energy than isomer 3I and exhibited a structure similar to those of isomers 3A and 3a. Isomer 3III, in which N_2 was bound to the Os atom in a side-on C_{2v} configuration with a $^2A_1$ electronic state, was 0.50 eV higher in energy than isomer 3I. The VDE and ADE values of isomers 3II (3.66 eV and 3.47 eV) and 3III (2.75 eV and 2.59 eV) differed from the experimental values. Moreover, the simulated spectrum of isomer 3I effectively reproduced the experimental spectrum (Fig. 3). The disagreement between the simulated spectra of isomers 3II and 3III and the experimental spectrum suggested that the presence of these isomers could be excluded.

Discussion

In the experimental spectrum, the spectral characteristics of MC_3^- and $MC_3N_2^-$ (M = Os, Ir) were clearly distinct; however, for PtC_3^- and $PtC_3N_2^-$, the resolved peaks were only red-shifted, and the spectral characteristics were extremely similar. These results suggested that nitrogen was present in $PtC_3N_2^-$ as a result of chemical adsorption and that $MC_3N_2^-$ (M = Os, Ir) exhibited a more specific nitrogen activation mode.

The agreement between the calculated and experimental results allowed the structure of the final product of the reaction between N_2 and MC_3^- (M = Os, Ir, Pt) to be determined. For $OsC_3N_2^-$, the most stable isomer observed in the experiment adopted a breaking configuration. For the $IrC_3N_2^-$ cluster, the isomers observed in the experiment adopted breaking and end-on configurations. However, for $PtC_3N_2^-$, the most stable isomer observed in the experiment adopted an end-on configuration. These results experimentally revealed the existence of two reaction modes between N_2 and MC_3^- (M = Os, Ir, Pt): breaking and end-on modes. Among them, two nitrogen activation mechanisms coexist in IrC_3^-, while OsC_3^- and PtC_3^- activate nitrogen by breaking the N≡N triple bond and chemisorption, respectively. Additionally, when the d orbital energy of the metal atom was lower, the end-on mode was more likely, corresponding to a lower degree of activation. Furthermore, the end-on configuration played an essential role as an

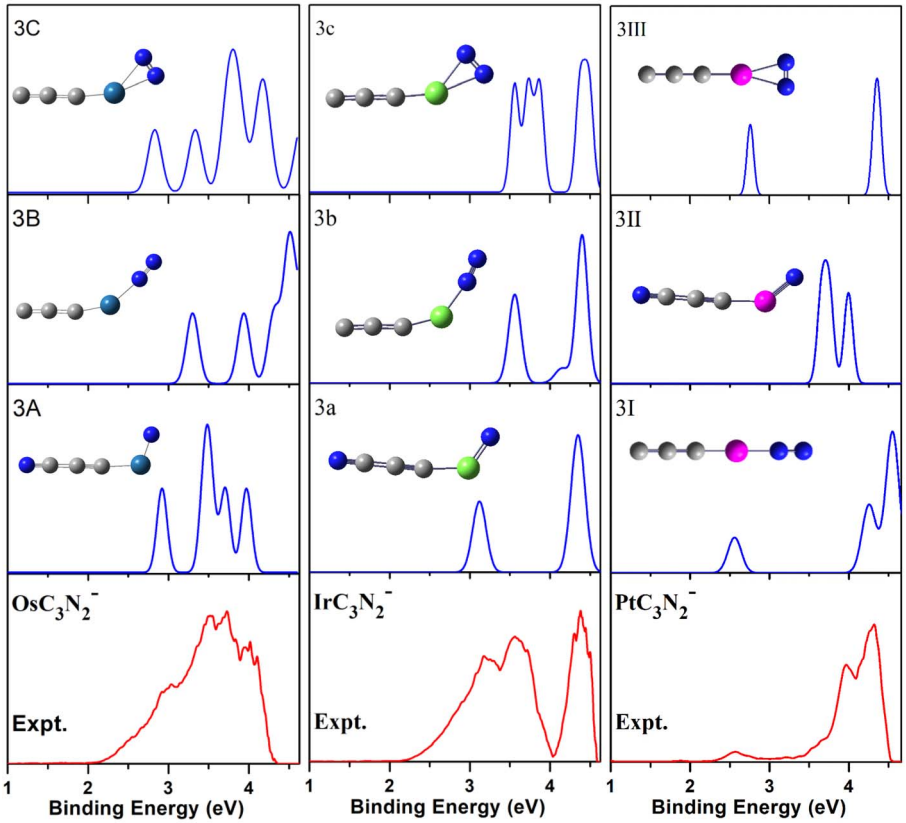

Fig. 3 Comparison of the experimental 266 nm photoelectron spectrum (red mark) of (M = Os, Ir, Pt) to the simulated spectra (blue mark) of the three low-lying isomers.

intermediate in the two reaction modes compared to the activation modes of MC_3^- (M = Os, Ir, Pt).

To explore the changes in the two modes of nitrogen activation for OsC_3^-, IrC_3^-, and PtC_3^-, we discussed in detail the bond length, Wiberg bond order, bond angle, NPA charges and CMO analysis of the products and intermediates (breaking configuration and end-on configuration) during the process.

The bond lengths and bond angles in these structures are listed in Fig. 4. The Wiberg bond orders between all atoms are listed in Table S1. Throughout the reaction, for the breaking configuration, the C–M–N bond angle (M = Os, Ir, Pt) increased sequentially for Os, Ir, and Pt. The M–N bond length of $OsC_3N_2^-$ (1.634 Å) was similar to that of $IrC_3N_2^-$ (1.658 Å), and the Pt–N bond length (1.748 Å) differed significantly from those of the Os–N and Ir–N bonds. The Wiberg bond orders of the M–N bonds were 2.730, 2.587, and 1.764 in the breaking configurations of $MC_3N_2^-$ with M = Os, Ir, and Pt, respectively, consistent with the variation in bond lengths. Furthermore, the bond lengths of the C–N bonds were 1.167 Å, 1.166 Å, and 1.164 Å, and the Wiberg bond orders of the C–N bonds were 2.656, 2.668 and 2.683, indicating the formation of relatively stable C–N bonds in the breaking configuration.

For the intermediate (end-on configuration), the N–N bond length increased from 1.095 Å (nitrogen molecule) to 1.120 Å ($OsC_3N_2^-$), 1.121 Å ($IrC_3N_2^-$), and 1.116 Å ($PtC_3N_2^-$). The Wiberg bond orders of the N–N bonds were 2.603, 2.596, and 2.642 in the end-on configuration of $MC_3N_2^-$ with M = Os, Ir, and Pt, respectively (Table S1), which were smaller than that of a free nitrogen molecule (3.000). These results revealed that the N–N bond was weakened, and the end-on configuration allowed a clear distinction among $PtC_3N_2^-$, $OsC_3N_2^-$, and $IrC_3N_2^-$: $PtC_3N_2^-$ exhibited a straight-chain end-on structure, whereas in $OsC_3N_2^-$ and $IrC_3N_2^-$, N_2 was bound to the Os and Ir atoms in an end-on configuration at a certain angle (148° and 140°). Moreover, to visualize the changes in the charges on these atoms, NPA was carried out (Table 2). Charge transfer occurred between MC_3^- (M = Os, Ir, Pt) and N_2, with the MC_3 groups transferring electrons to N_2. In the end-on configurations of $OsC_3N_2^-$ and $IrC_3N_2^-$, the negative charge on the N_2 group increased from 0 to −0.184 and −0.181, respectively, which was larger than the increase observed in the charge on the N_2 group (from 0 to −0.157) in $PtC_3N_2^-$. These results demonstrated that N_2 binding to metal atoms at a certain angle in the end-on configuration was more beneficial for the cleavage of the N≡N bond and that the activation of N_2 by MC_3^- decreased gradually for OsC_3^-, IrC_3^- and PtC_3^-.

Fig. S6 and 5 show the highest occupied molecular orbitals (HOMOs) of the breaking and end-on configurations of $MC_3N_2^-$ (M = Os, Ir, Pt), extending down to the sixth valence molecular orbital (MO) below the HOMO. The orbital compositions determined using the natural atomic orbital (NAO) method using the frontier Kohn–Sham (KS) MOs of these species are

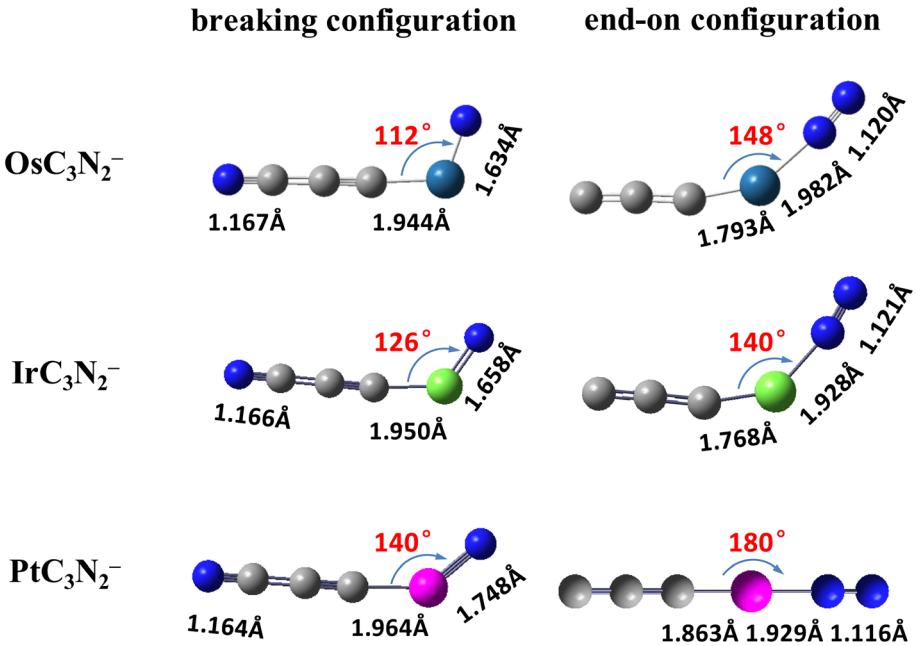

Fig. 4 The bond lengths and bond angles of the two low-energy isomers of $MC_3N_2^-$ (M = Os, Ir, Pt) were calculated at the B3LYP level.

Table 2 NPA charges of $MC_3N_2^-$ (M = Os, Ir, Pt) species calculated at the B3LYP level of theory

		NPA charges			
Cluster	Isomer	M	N (close to M)	N (far from M)	3C
$OsC_3N_2^-$	3A	−0.035	−0.332	−0.410	−0.222
	3B	−0.180	−0.128	−0.056	−0.663
$IrC_3N_2^-$	3a	−0.004	−0.367	−0.399	−0.230
	3b	−0.272	−0.106	−0.075	−0.547
$PtC_3N_2^-$	3I	−0.189	−0.095	−0.062	−0.653
	3II	−0.122	−0.482	−0.394	−0.247

shown in Tables S2–S7. In the breaking configuration, the HOMOs of $OsC_3N_2^-$ and $PtC_3N_2^-$ were singly occupied orbitals, whereas that of $IrC_3N_2^-$ was a doubly occupied MO. According to the distribution and proportion of orbitals, it was determined that many of the orbitals were consistent: the HOMOs of $OsC_3N_2^-$ (Os: 25% 5d + 25% 6s + 15% 6p; N: 27% 2p) and $IrC_3N_2^-$ (Ir: 27% 5d + 25% 6s + 6% 6p; N: 35% 2p), the HOMO-1 of $OsC_3N_2^-$ (Os: 70% 5d + 21% 6s), and the HOMO-2 of $IrC_3N_2^-$ (Ir: 74% 5d + 15% 6s), *etc.* $OsC_3N_2^-$ and $IrC_3N_2^-$ were found to be extremely similar, while $PtC_3N_2^-$ exhibited slight differences compared to $MC_3N_2^-$ (M = Os, Ir), indicating the specificity of nitrogen activation by MC_3^- (M = Os, Ir).

Previous investigations have demonstrated that π back-donation weakens N≡N bonds, which is crucial for the subsequent activation of N_2.[48,49] Overall, the majority of the π back-donation to N_2 originated from the 5d orbitals of the M atoms. In the intermediate, the N–N bond contributed to the HOMO, HOMO-1, HOMO-3, and HOMO-4 π antibonding (π*) orbitals of $OsC_3N_2^-$, and the contributions from these 5d Os

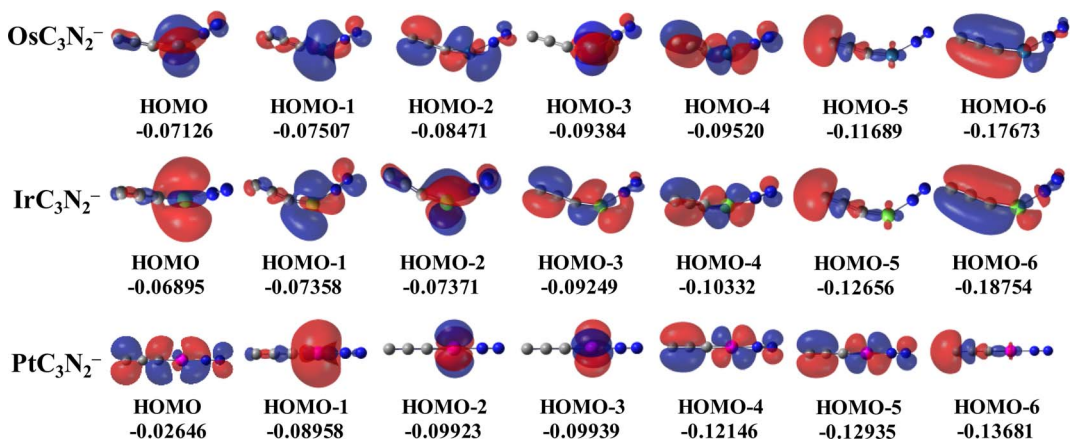

Fig. 5 Molecular orbital pictures of the end-on configuration of $MC_3N_2^-$ (M = Os, Ir, Pt) calculated at the B3LYP level of theory, showing the highest occupied molecular orbitals (HOMO) down to the sixth valence molecular orbital from the HOMO.

orbitals to the nitrogen antibonding orbitals were 94%, 43%, 92%, and 51%, respectively. The N–N bond contributed to the HOMO-1, HOMO-2, and HOMO-4 π* orbitals of $IrC_3N_2^-$, and the contributions from these 5d Ir orbitals were 64%, 91%, and 50%, respectively. The N–N bond contributed to the HOMO, HOMO-4, and HOMO-5 π* orbitals of $PtC_3N_2^-$, and the contributions from these 5d Ir orbitals were 7%, 54%, and 52%, respectively. These results indicated that the contribution from the 5d orbitals decreased from OsC_3^- to IrC_3^- and PtC_3^-, thus demonstrating that π back-donation decreased as the energy of the 5d orbitals decreased.

Conclusion

$MC_3N_2^-$ (M = Os, Ir, Pt) was prepared *via* a laser vaporization supersonic cluster source and was structurally characterized by photoelectron velocity-map imaging spectroscopy and quantum chemical calculations. The experimental results indicated the existence of two competing modes of nitrogen activation by the metal tricarbon clusters MC_3^- (M = Os, Ir, Pt): breaking and end-on modes. In this system, OsC_3^- cleaves the N≡N triple bond, IrC_3^- exhibits dual nitrogen activation mechanisms, and PtC_3^- fixes nitrogen in the end-on mode. The breaking mode generated stable C–N bonds, providing guidance for the application of C–N compounds, and the end-on mode involved nitrogen activation through chemisorption. Further calculations and analysis demonstrated that nitrogen activation by MC_3^- (M = Os, Ir, Pt) decreased as the 5d orbital energy of the metal atoms decreased, while the predominance of the end-on mode increased. These findings are promising for nitrogen activation and provide a basis for single-atom catalysis.

Author contributions

The experiments and theoretical analysis of the project were performed and written by S. D. and Z. Z., who also contributed equally to the manuscript. G. L. S. C. and X. K. directed the research and analyzed the data. L. L. Q. Y. and L. J. analyzed the results of the calculations. H. X. designed the project, supervised the research, and revised the manuscript. All authors discussed the results and contributed to the final version of the manuscript.

Conflicts of interest

The authors declare no conflict of interest.

Data availability

The data supporting this article have been included as part of the SI: optimized structures, molecular orbital pictures of the breaking configuration, bond lengths, Wiberg bond orders, and orbital composition analysis for $MC_3N_2^-$ (M = Os, Ir, Pt) complexes. See DOI: **https://doi.org/10.1039/d5sc04467g**.

Acknowledgements

This work was supported by the National Natural Science Foundation of China (grant no. 22273101, 22125303, 92061203, 22373102, and 22288201), the Youth Innovation Promotion Association of the Chinese Academy of Sciences (CAS) (2020187), the Innovation Program for Quantum Science and Technology (2021ZD0303304), the Scientific Instrument Developing Project of the Chinese Academy of Sciences (GJJSTD20220001), the International Partnership Program of the Chinese Academy of Sciences (121421KYSB20170012), and the Dalian Institute of Chemical Physics (DICP I202437). The authors gratefully acknowledge the staff members of the Dalian Coherent Light Source (31127.02.DCLS) for technical support and assistance in data collection.

References

1 D. V. Yandulov and R. R. Schrock, *Science*, 2003, **301**, 76–78.
2 K. Arashiba, Y. Miyake and Y. Nishibayashi, *Nat. Chem.*, 2010, **3**, 120–125.
3 J. S. Anderson, J. Rittle and J. C. Peters, *Nature*, 2013, **501**, 84–87.
4 J. W. Erisman, M. A. Sutton, J. Galloway, Z. Klimont and W. Winiwarter, *Nat. Geosci.*, 2008, **1**, 636–639.
5 X. D. W. W. Weare, M. J. Byrnes, J. M. Chin, R. R. Schrock and P. Muller, *Proc. Natl. Acad. Sci. U. S. A.*, 2006, **103**, 17099–17106.
6 L.-H. Mou, Z.-Y. Li and S.-G. He, *J. Phys. Chem. Lett.*, 2022, **13**, 4159–4169.
7 N. Kuganathan, H. Hosono, A. L. Shluger and P. V. Sushko, *J. Am. Chem. Soc.*, 2014, **136**, 2216–2219.
8 J. M. P. Martirez and E. A. Carter, *ACS Nano*, 2016, **10**, 2940–2949.
9 M. Falcone, L. Chatelain, R. Scopelliti, I. Živković and M. Mazzanti, *Nature*, 2017, **547**, 332–335.
10 C. Cui, H. Zhang, R. Cheng, B. Huang and Z. Luo, *ACS Catal.*, 2022, **12**, 14964–14975.
11 M.-A. Légaré, G. Bélanger-Chabot, R. D. Dewhurst, E. Welz, I. Krummenacher, B. Engels and H. Braunschweig, *Science*, 2018, **359**, 896–900.
12 X.-L. Ma, J.-C. Liu, H. Xiao and J. Li, *J. Am. Chem. Soc.*, 2018, **140**, 46–49.
13 A. McSkimming and D. L. M. Suess, *Nat. Chem.*, 2021, **13**, 666–670.
14 X. Peng, H.-X. Liu, Y. Zhang, Z.-Q. Huang, L. Yang, Y. Jiang, X. Wang, L. Zheng and C. Chang, *Chem. Sci.*, 2021, **12**, 7125–7137.
15 E. C. Tyo and S. Vajda, *Nat. Nanotechnol.*, 2015, **10**, 577–588.
16 F. Fu, J. Xiang, H. Cheng, L. Cheng, H. Chong, S. Wang, P. Li, S. Wei, M. Zhu and Y. Li, *ACS Catal.*, 2017, **7**, 1860–1867.
17 X. Cheng, Z.-Y. Li, G.-D. Jiang, X.-X. Liu, Q.-Y. Liu and S.-G. He, *J. Phys. Chem. Lett.*, 2023, **14**, 6431–6436.
18 Y.-Q. Ding, F.-X. Zhang, Y. Li and J.-B. Ma, *J. Phys. Chem. A*, 2024, **128**, 449–455.
19 H.-J. Himmel, O. Hubner, W. Klopper and L. Manceron, *Angew. Chem., Int. Ed.*, 2006, **45**, 2799–2802.

20 Y. Gong, Y. Zhao and M. Zhou, *J. Phys. Chem. A*, 2007, **111**, 6204–6207.
21 M. Zhou, X. Jin, Y. Gong and J. Li, *Angew. Chem., Int. Ed.*, 2007, **46**, 2911–2914.
22 C. Geng, J. Li, T. Weiske and H. Schwarz, *Proc. Natl. Acad. Sci. U. S. A.*, 2018, **115**, 11680–11687.
23 Y. Zhao, J.-T. Cui, M. Wang, D. Y. Valdivielso, A. Fielicke, L.-R. Hu, X. Cheng, Q.-Y. Liu, Z.-Y. Li, S.-G. He and J.-B. Ma, *J. Am. Chem. Soc.*, 2019, **141**, 12592–12600.
24 C. Geng, J. Li, T. Weiske and H. Schwarz, *Proc. Natl. Acad. Sci. U. S. A.*, 2019, **116**, 21416–21420.
25 X. Cheng, Z.-Y. Li, L.-H. Mou, Y. Ren, Q.-Y. Liu, X.-L. Ding and S.-G. He, *Chem.–Eur. J.*, 2019, **25**, 16523–16527.
26 Y. Li, L.-H. Mou, G.-D. Jiang, Z.-Y. Li, S.-G. He and H. Chen, *Inorg. Chem.*, 2024, **63**, 10775–10785.
27 H.-J. Himmel and M. Reiher, *Angew. Chem., Int. Ed.*, 2006, **45**, 6264–6288.
28 J. Li, C. Geng, T. Weiske and H. Schwarz, *Angew. Chem., Int. Ed.*, 2020, **59**, 9370–9376.
29 C. Geng, T. Weiske, J. Li, S. Shaik and H. Schwarz, *J. Am. Chem. Soc.*, 2018, **141**, 599–610.
30 X. Liu, G. Li, Z. Liu, W. Yang, H. Fan, L. Jiang and H. Xie, *J. Phys. Chem. Lett.*, 2022, **13**, 12–17.
31 Y. Zhang, S. Du, Z. Zhao, H. Han, G. Li, J. Zou, H. Xie and L. Jiang, *J. Energy Chem.*, 2023, **77**, 529–534.
32 Z.-Y. Li, L.-H. Mou, G.-P. Wei, Y. Ren, M.-Q. Zhang, Q.-Y. Liu and S.-G. He, *Inorg. Chem.*, 2019, **58**, 4701–4705.
33 Z.-Y. Li, Y. Li, L.-H. Mou, J.-J. Chen, Q.-Y. Liu, S.-G. He and H. Chen, *J. Am. Chem. Soc.*, 2020, **142**, 10747–10754.
34 L.-H. Mou, Y. Li, Z.-Y. Li, Q.-Y. Liu, Y. Ren, H. Chen and S.-G. He, *J. Phys. Chem. Lett.*, 2020, **11**, 9990–9994.
35 L.-H. Mou, Y. Li, Z.-Y. Li, Q.-Y. Liu, H. Chen and S.-G. He, *J. Am. Chem. Soc.*, 2021, **143**, 19224–19231.
36 Y.-Y. Wang, X.-L. Ding, J. I. Gurti, Y. Chen, X.-Q. Huang, W. Li and X. Wang, *ChemPhysChem*, 2021, **23**, e202100771.
37 Z.-Y. Li, F. Horn, Y. Li, L.-H. Mou, W. Schöllkopf, H. Chen, S.-G. He and K. R. Asmis, *Chem.–Eur. J.*, 2023, **29**, e202203384.
38 C. Chen, X. Zhu, X. Wen, Y. Zhou, L. Zhou, H. Li, L. Tao, Q. Li, S. Du, T. Liu, D. Yan, C. Xie, Y. Zou, Y. Wang, R. Chen, J. Huo, Y. Li, J. Cheng, H. Su, X. Zhao, W. Cheng, Q. Liu, H. Lin, J. Luo, J. Chen, M. Dong, K. Cheng, C. Li and S. Wang, *Nat. Chem.*, 2020, **12**, 717–724.
39 Z.-Y. Chen, M. Wang and J.-B. Ma, *Chem.–Eur. J.*, 2022, **28**, e202201170.
40 L.-Y. Chu, Y.-Q. Ding, M. Wang and J.-B. Ma, *Phys. Chem. Chem. Phys.*, 2022, **24**, 14333–14338.
41 Y.-Q. Ding, Y. Li, F. Ying, M. Wang and J.-B. Ma, *J. Phys. Chem. Lett.*, 2022, **13**, 492–497.
42 Z. Qin, X. Wu and Z. Tang, *Rev. Sci. Instrum.*, 2013, **84**, 066108.
43 Z. Qin, R. Cong, X. Wu, Z. Liu, H. Xie, Z. Tang, L. Jiang and H. Fan, *J. Chem. Phys.*, 2013, **139**, 034315.
44 M. J. Frisch, G. W. Trucks, H. B. Schlegel, G. E. Scuseria, M. A. Robb, J. R. Cheeseman, G. Scalmani, V. Barone, B. Mennucci, G. A. Petersson, H. Nakatsuji, M. Caricato, X. Li, H. P. Hratchian, A. F. Izmaylov, J. Bloino, G. Zheng, J. L. Sonnenberg, M. Hada, M. Ehara, K. Toyota, R. Fukuda, J. Hasegawa, M. Ishida, T. Nakajima, Y. Honda, O. Kitao, H. Nakai, T. Vreven, J. A. Montgomery Jr, J. E. Peralta, F. Ogliaro, M. J. Bearpark, J. Heyd, E. N. Brothers, K. N. Kudin, V. N. Staroverov, R. Kobayashi, J. Normand, K. Raghavachari, A. P. Rendell, J. C. Burant, S. S. Iyengar, J. Tomasi, M. Cossi, N. Rega, N. J. Millam, M. Klene, J. E. Knox, J. B. Cross, V. Bakken, C. Adamo, J. Jaramillo, R. Gomperts, R. E. Stratmann, O. Yazyev, A. J. Austin, R. Cammi, C. Pomelli, J. W. Ochterski, R. L. Martin, K. Morokuma, V. G. Zakrzewski, G. A. Voth, P. Salvador, J. J. Dannenberg, S. Dapprich, A. D. Daniels, O. Farkas, J. B. Foresman, J. V. Ortiz, J. Cioslowski and D. J. Fox, *Gaussian 09*, Gaussian, Inc., Wallingford, CT, USA, 2009.
45 C. Lee, W. Yang and R. G. Parr, *Phys. Rev. B*, 1988, **37**, 785–789.
46 J. T. H. Dunning, *J. Chem. Phys.*, 1989, **90**, 1007–1023.
47 A. D. Becke, *J. Chem. Phys.*, 1993, **98**, 5648–5652.
48 S. Du, X. Liu, B. Ju, J. Zhang, J. Zou, G. Li, H. Fan, H. Xie and L. Jiang, *Inorg. Chem.*, 2022, **62**, 170–177.
49 S. Du, X. Liu, Z. Liu, G. Li, H. Fan, H. Xie and L. Jiang, *JACS Au*, 2023, **3**, 1723–1727.